Open Access

Earth System
Science
Data

Discussions

Development of a global 30-m impervious surface map using multi-source and multi-temporal remote sensing datasets with the Google Earth Engine platform

Xiao Zhang[1, 2], Liangyun Liu[1, 2], Changshan Wu[3], Xidong Chen[1, 2], Yuan Gao[1, 4], Shuai Xie[1, 2] and Bing Zhang[1, 2]

[1] State Key Laboratory of Remote Sensing Science, Institute of Remote Sensing and Digital Earth, Chinese Academy of Sciences, Beijing 100094, China
[2] University of Chinese Academy of Sciences, Beijing 100049, China
[3] Department of Geography, University of Wisconsin-Milwaukee, Milwaukee, WI, USA
[4] College of Geometrics, Xi'an University of Science and Technology, Xi'an 710054, China

Correspondence to: Liangyun Liu (liuly@radi.ac.cn)

Abstract. The amount of impervious surface is an important indicator in the monitoring of the intensity of human activity and environmental change. The use of remote sensing techniques is the only means of accurately carrying out global mapping of impervious surfaces covering large areas. Optical imagery can capture surface reflectance characteristics, while synthetic aperture radar (SAR) images can be used to provide information on the structure and dielectric properties of surface materials. In addition, night-time light (NTL) imagery can detect the intensity of human activity and thus provide important a priori probabilities of the occurrence of impervious surfaces. In this study, we aimed to generate an accurate global impervious surface map at a resolution of 30-m for 2015 by combining Landsat-8 OLI optical images, Sentinel-1 SAR images and VIIRS NTL images based on the Google Earth Engine (GEE) platform. First, the global impervious and non-impervious training samples were automatically derived by combining the GlobeLand30 land-cover product with VIIRS NTL and MODIS enhanced vegetation index (EVI) imagery. Then, based on global training samples and multi-source and multi-temporal imagery, a random forest classifier was trained and used to generate corresponding impervious surface maps for each 5°×5° cell of a geographical grid. Finally, a global impervious surface map, produced by mosaicking numerous 5°×5° regional maps, was validated by interpretation samples and then compared with three existing impervious products (GlobeLand30, FROM_GLC and NUACI). The results indicated that the global impervious surface map produced using the proposed multi-source, multi-temporal random forest classification (MSMT_RF) method was the most accurate of the maps, having an overall accuracy of 96.6% and kappa coefficient of 0.903 as against 92.5% and 0.769 for FROM_GLC, 91.1% and 0.717 for GlobeLand30, and 87.43% and 0.585 for NUACI. Therefore, it is concluded that a global 30-m impervious surface map can accurately and efficiently be generated by the proposed MSMT_RF method based on the GEE platform. The global impervious surface map generated in this paper are available at https://doi.org/10.5281/zenodo.3505079 (Zhang and Liu, 2019).

1 Introduction

Impervious surfaces are usually covered by anthropogenic materials which prevent water penetrating into the soil (Weng, 2012). Impervious surfaces include asphalts, sand and stone, concrete, bricks, glasses, etc. (Chen et al., 2015). Due to the rapid growth in the area covered by impervious surfaces, a series of climate, environmental and social problems are emerging,

35 including the urban heat island, traffic congestion, waterlogging and the deterioration of urban the environment (Fu and Weng, 2016; Gao et al., 2012; Weng, 2001; Zhou et al., 2017; Zhuo et al., 2018). Furthermore, as an important indicator in the monitoring of the intensity of human activity and of ecological and environmental changes, the mapping of impervious surfaces is of great interest in many disciplines (Xie and Weng, 2017). Accurate large-area impervious surface mapping is, therefore, urgent and necessary.

40 Due to the frequent and large-area coverage that it provides, increasing attention has been paid to the use of remote sensing technology for impervious surface mapping. In recent years, a lot of effort has gone into mapping impervious surfaces at different spatial resolutions (Chen et al., 2015; Elvidge et al., 2007; Liu et al., 2018; Schneider et al., 2010; Schneider et al., 2009). For example, Schneider et al. (2010) used multi-temporal MODIS data to produce a 500-m global urban land map, achieving an overall accuracy of 93% and kappa coefficient of 0.65. Elvidge et al. (2007) combined the Defense Meteorological

45 Satellite Program (DMSP) Operational Linescan System (OLS) and LandScan population count data to produce a 1-km global impervious surface area map. However, Gao et al. (2012) explained that these coarse-resolution global impervious surface maps were not suitable for many applications and policy makers at local or regional scales. Recently, with the advent of free medium-resolution satellite data (e.g. Landsat and Sentinel-2), combined with rapidly-increasing data-storage and computation capabilities, many regional or global fine-resolution impervious surface maps have been produced using Landsat and Sentinel-

50 2 images (Chen et al., 2015; Gao et al., 2012; Goldblatt et al., 2018; Gong et al., 2019; Gong et al., 2013; Homer et al., 2015; Li et al., 2018; Liu et al., 2018; Sun et al., 2017). Specifically, the National Land Cover Dataset (NLCD) produced the first 30-m map of the United States including impervious surface as a separate land-cover type using Landsat imagery (Homer et al., 2004). Similarly, the FROM_GLC and GlobeLand30 products also produced the global 30-m impervious surface map as an independent land cover type (Chen et al., 2015; Gong et al., 2013). However, these land-cover products focus on the overall

55 accuracy of the mapping of all land-cover types rather than that of impervious surfaces alone. Latterly, Liu et al. (2018) proposed the Normalized Urban Areas Composite Index (NUACI) method for producing a global 30-m impervious surface map and achieved an overall accuracy of 0.81-0.84 and a kappa values of 0.43-0.50. However, the NUACI product had a relatively poor performance in terms of producer's accuracy (0.50–0.60) and user's accuracy (0.49-0.61). Therefore, an accurate impervious surface map at fine spatial resolution is still urgently needed.

60 There are three critical challenges for global impervious surface mapping at medium spatial resolution. These include finding an adequate image identification method, image selection scheme and image processing platform (Liu et al., 2018).

First, although a wide range of methods have already been presented for impervious surface mapping, it is still hard to generate an operational and accurate global impervious surface map at 30-m resolution. The methods used so far can be divided into three main groups: spectral mixture analysis methods (Ridd, 1995; Wetherley et al., 2017; Wu, 2004; Wu and Murray, 2003; Yang and He, 2017; Zhuo et al., 2018), spectral index-based methods (Deng and Wu, 2012; Liu et al., 2018; Xu, 2010), and image classification methods (Chen et al., 2015; Okujeni et al., 2013; Zhang et al., 2018a; Zhang et al., 2012; Zhang and Weng, 2016). The spectral mixture analysis methods have great advantages in terms of the repeatable and accurate extraction of quantitative sub-pixel information (Weng, 2012). However, these spectral mixture methods can produce underestimates in areas whether the density of impervious surfaces is high and overestimates in areas of low density (Sun et al., 2017; Weng, 2012). The spectral index-based methods have been widely applied in regional impervious surface mapping due to their simplicity, flexibility and convenience (Liu et al., 2018; Sun et al., 2019b; Xu, 2010). However, the spectral index-based methods have great difficulty in finding the optimal threshold for separating the impervious pixels from bare areas and vegetation pixels (Sun et al., 2017). The image classification methods can efficiently combine remote sensing datasets from multiple sources (Zhang et al., 2016; Zhang et al., 2018a; Zhou et al., 2017) and have great capabilities in spectrally complex impervious surface mapping (Okujeni et al., 2013), which has been an area of great interest in recent years (Goldblatt et al., 2018; Zhang et al., 2018b). However, it is very hard to select training samples for large-area impervious surface mapping using these methods (Weng, 2012).

Second, although individual optical data sets have been successfully employed for regional or global impervious surface mapping, accurate estimation of impervious surfaces remains challenging due to the diversity of urban land-cover types, which leads to difficulties in separating different land-cover types with similar spectral signatures (Zhang et al., 2014b). The incorporation of multi-source and multi-temporal remote sensing imagery has been demonstrated to improve impervious surface mapping accuracy (Weng, 2012; Zhu et al., 2012). For example, optical imagery is only able to capture surface reflectance characteristics, while synthetic aperture radar (SAR) data can provide details of the structure and dielectric properties of the surface materials (Sun et al., 2019b; Zhang et al., 2014b; Zhu et al., 2012). Zhang et al. (2016) found that the addition of dual-polarimetric SAR features resulted in an accuracy improvement of 3.5% compared with using optical SPOT-5 imagery only and also that dual-polarimetric SAR data had a superior performance to single polarimetric SAR data for impervious mapping. Similarly, Shao et al. (2016) explained that the combination of GaoFen-1 optical imagery with Sentinel-1 SAR imagery efficiently reduced the confusion between impervious surfaces and water and bare areas. Furthermore, Zhu et al. (2012) found that the inclusion of multi-seasonal imagery increased the mapping accuracy from 77.96% to 86.86% and that the further addition of texture variables increased the mapping accuracy to 92.69% for urban and peri-urban land-cover classification. The reasons for the accuracy increase were that the texture imagery could capture the local spatial structure and the variability in land cover categories and also that the temporal information could describe the phenological variability. Schug et al. (2018) also used the multi-seasonal Landsat imagery to successfully map impervious extent and land cover fractions. In addition, as an important data source for the measurement of socioeconomic activities, DMSP-OLS night-time

Earth System
Science
Data

Open Access

Discussions

95   light (NTL) imagery have been widely used in many impervious-related applications (Li and Zhou, 2017). For example, Elvidge et al. (2007) successfully produced a global 1-km impervious map using DMSP-OLS NTL imagery, Goldblatt et al. (2018) combined DMSP-OLS NTL and Landsat-8 imagery to accurately produce 30-m impervious surface maps at a national scale. Therefore, the integration of multi-source and multi-temporal datasets is necessary and crucial to the production of accurate global impervious surface maps.

100   Lastly, the mapping of impervious surfaces at the global scale usually requires huge amounts of computation and large storage capabilities. Fortunately, the Google Earth Engine (GEE) cloud-based platform consists of a multi-petabyte analysis-ready data catalog co-located with a high-performance, intrinsically parallel computation service (Gorelick et al., 2017), meaning that the requirements for large-area image collection and very large computational resources can easily be met by using the free-access GEE cloud-computation platform. For example, Liu et al. (2018) produced multi-temporal global impervious

105   surface maps and Pekel et al. (2016) developed global high-resolution surface water maps and analyzed long-term changes using the GEE cloud-computation platform. Recently, Massey et al. (2018) produced a continental-scale cropland extent map for North America at 30 m spatial resolution for the nominal year 2010 based on the GEE platform. It can be seen, therefore, that the GEE is an efficient and useful computation platform for regional/global applications.

So far, due to the limitations of data collection and computation capability, impervious surface mapping has mainly focused

110   on using a single type of remote sensing data or on case studies made at the regional scale. Although the GEE platform provides multi-petabyte analysis-ready data and efficient data-processing capabilities, an efficient method that can fully integrate these multi-source and multi-temporal datasets and produce accurate impervious surface maps at a spatial resolution of 30-m for the whole world is still lacking. The aims of this study, therefore, were (1) to produce a global 30-m impervious surface map from multi-source multi-temporal remote sensing datasets including Landsat-8 OLI, Sentinel-1 SAR, VIIRS NTL and MODIS

115   imagery using the GEE platform; (2) to investigate the accuracy of the global 30-m impervious surface mapping using validation samples and cross-comparison with three existing impervious surface products (GlobeLand30 (Chen et al., 2015), FROM_GLC (Gong et al., 2013) and NUACI (Liu et al., 2018)). The results indicate that the global impervious surface map produced by the proposed method is accurate and is suitable for regional or global impervious surface applications.

2 Datasets

120   **2.1 Remote sensing datasets**

In this study, five kinds of data sources including Landsat-8 optical imagery, Sentinel-1 SAR data, VIIRS NTL imagery and MODIS EVI imagery, as well as STRM/ASTER DEM topographical variables, were selected and collected for the mapping of impervious surfaces across the world using the GEE platform.

All available Landsat-8 surface reflectance (SR) imagery from 2015 and 2016(USGS, 2015), which had been archived on the
125   GEE platform, were used in this study for the nominal year 2015 because of the frequent cloud contamination in the tropic
areas. All the SR images were radiometrically corrected by the Landsat Surface Reflectance Code (LaSRC) atmospheric
correction method (Hu et al., 2014; Vermote et al., 2016), and bad pixels including clouds, cloud shadow, and saturated pixels
were identified by the CFMask algorithm (Guide, 2018).

The Sentinel-1 satellite provides C-band SAR imagery at a variety of polarizations and resolutions, and the repeat cycle of the
130   polar-orbiting two-satellite constellation is 6 days (Berger et al., 2012; ESA, 2016; Torres et al., 2012). In this study, all
available Sentinel-1 imagery from 2015 and 2016, which had already been calibrated and ortho-corrected then archived on the
GEE platform, were also used for the nominal year 2015. In addition, each Sentinel-1 image on the GEE had been pre-
processed with the Sentinel-1 Toolbox, including thermal noise removal, radiometric calibration and terrain correction
(https://developers.google.com/earth-engine/sentinel1). Also, as HH- and HV-polarized Sentinel-1 SAR imagery does not
135   cover the whole world (Sun et al., 2019a), a combination of dual-band cross-polarized (VV and VH) Interferometric Wide
Swath (IW) mode imagery in both 'ascending' and 'descending' orbits was used. The spatial resolution of this imagery was
10-m.

The VIIRS NTL, collected by NASA/NOAA's Suomi National Polar-orbiting Partnership satellite
(https://maps.ngdc.noaa.gov/viewers/VIIRS_DNB_nighttime_imagery/index.html), has the unique ability to record emitted
140   visible and near-infrared (VNIR) radiation at night with a spatial resolution of 15 arc seconds (equivalent to 0.5 km at the
equator) (Elvidge et al., 2017). Compared to the DMSP-OLS NTL data, the VIIRS NTL data provide higher spatial resolution,
and finer radiometric resolution, which allows weaker surface radiation to be detected (Bennett and Smith, 2017). It is also the
main data source used for studying the expansion of impervious surfaces and related sociodemographic issues (Elvidge et al.,
2017). In this study, a combination of VIIRS NTL, MODIS EVI imagery and GlobeLand30 land-cover products was used to
145   derive the set of global training samples.

The MODIS EVI imagery (MYD13Q1) from the MODIS V6 products contains the best available EVI data from among all
the acquisitions obtained over a 16-day compositing period. The imagery has a spatial resolution of 250-m (Didan et al., 2015).
In this study, the EVI imagery for 2015 in the GEE used the blue band to remove residual atmospheric contamination caused
by smoke and sub-pixel thin clouds (https://developers.google.com/earth-engine/datasets/catalog/ MODIS_006_MYD13Q1).

150   The last data source used was the Shuttle Radar Topography Mission digital elevation model (SRTM DEM), provided by the
NASA JPL at a resolution of 1 arc-second (approximately 30 m) and covering the area between 60° north and 56° south (Farr
et al., 2007). This dataset has undergone a void-filling process using other open-source data (ASTER GDEM2, GMTED2010
and NED) in the GEE platform. As for the high-latitude areas that lacked the SRTM data, the Advanced Spaceborne Thermal
Emission and Reflection Radiometer (ASTER) Global Digital Elevation Model Version 2 (GDEM V2) (Tachikawa et al.,
155   2011) was used instead.

2.2 Global impervious surface products

In this study, three global impervious surface products − GlobeLand30, FROM_GLC and NUACI − were used to validate the global impervious surface map produced using the MSMT_RF method. The GlobeLand30 data were also used to automatically derive the global impervious and non-impervious training samples.

160 GlobeLand30 is an operational 30-m global land-cover dataset produced using the Pixel-Object-Knowledge-based method (POK-based) approach in 2000 and 2010 (Chen et al., 2015). In this study, the global impervious product derived from GlobeLand30 in 2010 (GlobeLand30-2010) was selected (http://www.globallandcover.com/ GLC30Download/index.aspx). The impervious surface land-cover type in GlobeLand30-2010 has been validated as having a user's accuracy of 86.7%.

FROM_GLC, first produced in 2010, was the first 30-m resolution global land-cover dataset and was produced by supervised
165 classification of 8,900 Landsat images (Gong et al., 2013). In this study, the second generation of FROM_GLC from 2015 (FROM_GLC2015) (http://data.ess.tsinghua.edu.cn/) was used. This dataset was produced by using multi-seasonal Landsat imagery acquired between 2013 and 2015 and incorporates the day of year, geographical coordinates and elevation data (Li et al., 2017).

The NUACI-based maps, developed using the spectral index-based method applied to Landsat and DMSP-OLS NTL imagery,
170 are multi-temporal global 30-m impervious surface datasets (Liu et al., 2018). In this study, the NUACI impervious map from 2015 (NUACI_2015) was used (http://www.geosimulation.cn/ GlobalUrbanLand.html). This map has been validated as having an overall accuracy of 0.81–0.84 and kappa coefficient of 0.43–0.50 at the global level (Liu et al., 2018).

2.3 Validation samples

To quantitatively assess the performance of the global impervious surface map, twelve $1° × 1°$ validation regions (blue
175 rectangles), including five high-density, four medium-density and three low-density regions, were randomly selected based on the density and distribution of the impervious surfaces (Fig. 1). For each validation region, 600-1000 samples were randomly generated using the stratified random sampling strategy (Bai et al., 2015). As there were significant advantages to using Google Earth for validation sample selection (Zhang et al., 2018c), each sample was labeled either as "non-impervious surface" or "impervious surface" based on visual interpretation of the available high-resolution remote sensing imagery in Google Earth.
180 In addition, to ensure the reliability of each validation sample, the location of each sample was moved to the center of the relevant surface object (building, road, etc.) because of the greater spectral mixing effect and uncertainty at the boundary of the objects. Like the work of Sun et al. (2019b), if the impervious area in the 30-m ×30-m validation window was more than a predefined threshold of 50%, we will consider this validation point as impervious surface, otherwise, it would be labeled as non-impervious surface. After careful interpretation, a total of 10,142 samples including 2381 impervious samples and 7761
185 non-impervious samples were obtained. In order to minimize the subjective influence of interpretation, the validation samples

were collected independently by three different scientists. If there was dispute between the interpretation results of three scientists, the validation point was discarded.
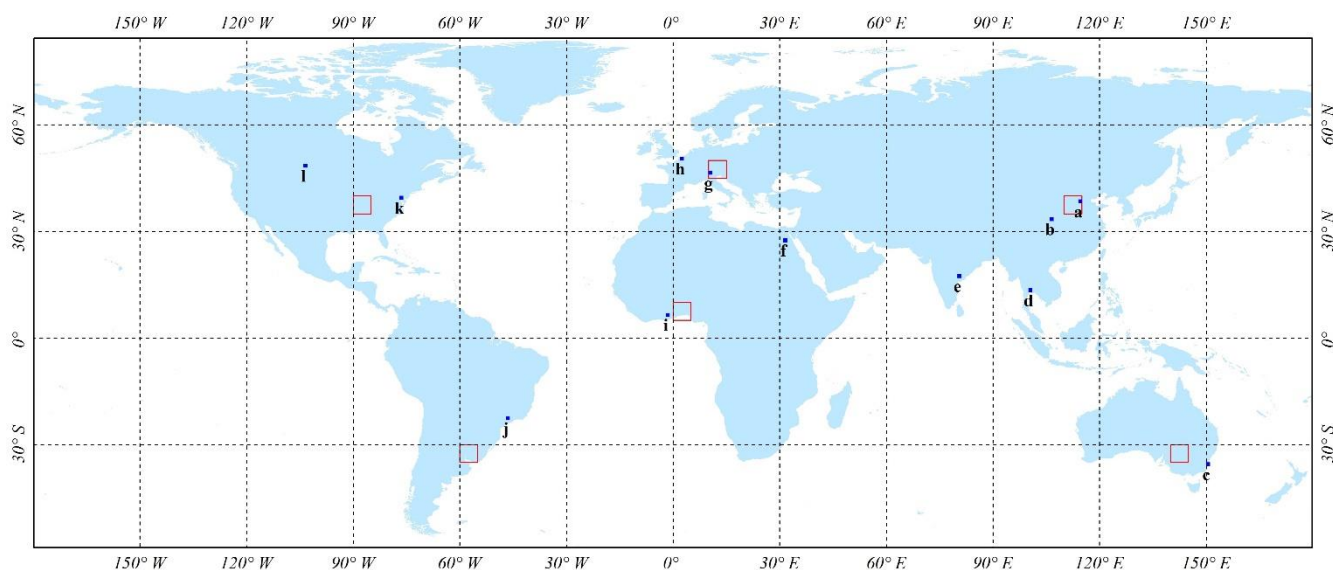

Figure 1: The spatial distribution of twelve 1°×1° validation regions (blue) corresponding to regions of different impervious surface density on different continents together with six 5°×5° validation regions (red) used to measure the variable importance.

3 Methods

To develop the global 30-m impervious surface map for 2015, the multi-source and multi-temporal random forest classification (MSMT_RF) method was proposed. The method is illustrated in Fig. 2. First, time series of Landsat-8 SR and Sentinel-1 SAR imagery archived on the GEE platform were collected. Secondly, the temporal–spectral–textural features and temporal–SAR features were derived from the Landsat-8 and Sentinel-1 imagery using image compositing methods. Thirdly, based on the GlobeLand30-2010 impervious surface products, and the VIIRS NTL and MODIS EVI imagery, the global impervious and non-impervious training samples were automatically generated. The random forest classifier was trained at each 5°×5° geographical grid cell using the temporal–spectral–textural–SAR-topographical features and the global training samples. Finally, the global impervious surface map was compared with three existing impervious surface products and further validated using the visual interpretation samples.

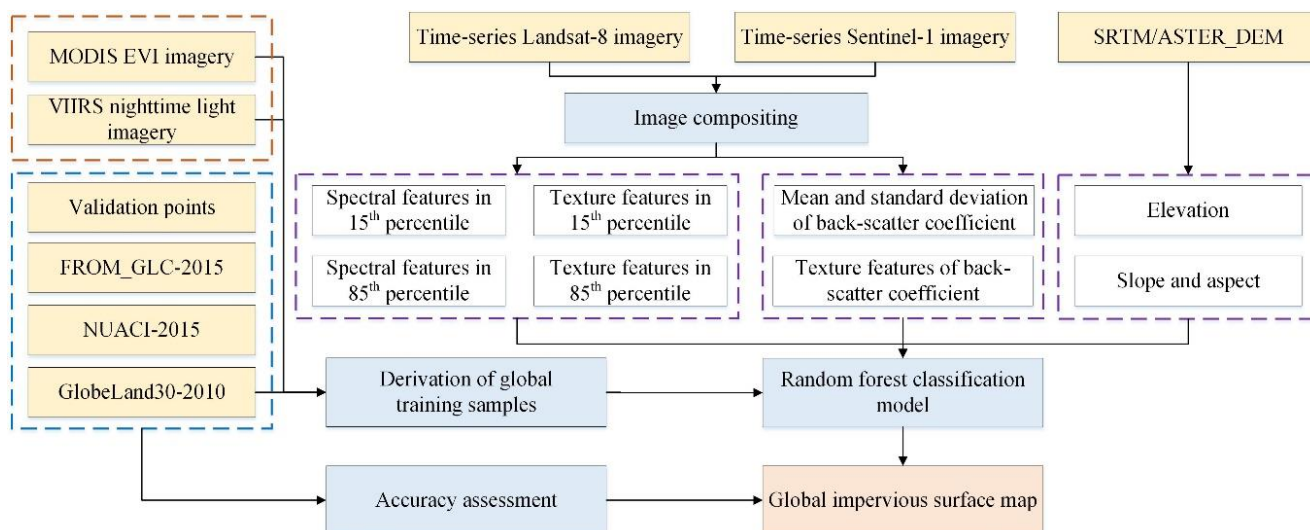Figure 2: Flowchart illustrating the MSMT_RF method.

3.1 Derivation of global training samples from GlobeLand30-2010

As the reliability and representativeness of the training samples would affect the classification accuracy directly (Foody and
205 Mathur, 2004), we proposed using the multi-source datasets to derive accurate impervious and non-impervious samples. It was
assumed that the process of transforming non-impervious surfaces into impervious surfaces was irreversible during the period
2010 to 2015, meaning that the global training samples derived from GlobeLand30-2010 could also be used to represent the
situation in 2015.

First, as GlobeLand30 used an object-based labeling method to remove the "salt-and-pepper effect" caused by the pixel-based
210 classification method (Chen et al., 2015), the impervious surfaces consisted of independent blocks. Usually, a large number of
mixed pixels and misclassifications occur at the boundary of image blocks or objects, and Yang et al. (2017) also found that
GlobeLand30 exhibited higher accuracy in homogeneous areas. The land-cover heterogeneity was calculated as the number of
land-cover types occurring in a local window (Jokar Arsanjani et al., 2016). According to the statistics of Chen et al. (2015),
there were a little commission and omission errors in each scene when the area of impervious surface block was less than 8×8.
215 In this study, the local window size was set to 9×9 after balancing the sample reliability and completeness because the higher
window size would cause the candidate samples miss those small and broken impervious objects (such as: rural villages).
Therefore, if the land-cover heterogeneity in the 9×9 local window was greater than 1 (meaning that the land-cover types
within the window consisted of both impervious and non-impervious types), the center pixel was removed from the candidate
training point set (CanTPS_Imp).

220 Secondly, to minimize the effects of mapping error in GlobeLand30-2010 and temporal interval between GlobeLand30-2010
and the input imagery for training samples in CanTPS_Imp, the VIIRS NTL data, revealed the intensity of socioeconomic
activities, was imported to refine each training point in 2015. However, as the coarse spatial resolution of VIIRS NTL imagery

might cause a 'blooming effect' in suburban areas, the EANTLI proposed by Zhuo et al. (2018) was applied to reduce the blooming effects:

225 $$EANTLI = \frac{1+(NTL_{norm}-EVI)}{1-(NTL_{norm}-EVI)} \times NTL \ , \tag{1}$$

where NTL_{norm} is the normalized NTL value, EVI is the annual mean value of the time-series MODIS EVI products and NTL is the actual value of the VIIRS NTL data.

The EANTLI measured the likelihood of the pixel corresponding to an impervious surface, so it was reasonable to assume that the pixels where EANTLI exceeded a certain threshold were impervious surface pixels. In this study, as the candidate training

230 points in CanTPS_Imp were collected from homogenous 9×9 pixel areas (270 m×270 m), the EANTLI image in 2015 (EANTLI-2015) was first resampled to the 270 m to match with these candidate points. The GlobeLand30-2010 impervious surface map had a user's accuracy of 86.7%, and we assumed that the process of transforming non-impervious surfaces into impervious surfaces was irreversible during the period 2010 to 2015, so the impervious segmentation threshold was selected as being the lowest 15th quantile of the cumulative probability of all candidate impervious points for EANTLI-2015; namely,

235 if the cumulative probability of the impervious point in CanTPS_Imp was lower than the threshold, the candidate point was removed from CanTPS_Imp. As for the non-impervious pixels, there was usually a negative correlation between non-impervious surfaces and EANTLI values, and the non-impervious surface samples turned into impervious surface would reflect the high EANTLI-2015 values, so if the cumulative probability of a candidate non-impervious point in CanTPS_Imp was greater than the top 20th percentile of the cumulative probability of all candidate non-impervious points (the threshold being

240 based on the overall accuracy of 80.33% for GlobeLand30-2010 and a little potential conversion samples), the candidate non-impervious point was also removed.

Lastly, although the candidate training points were refined using the GlobeLand30-2010 and EANTLI-2015 imagery, the volume of candidate training points was still huge and so it was necessary to further resample the CanTPS_Imp. Based on the work of Jin et al. (2014), who investigated the impact of training sample selection on the impervious classification accuracy,

245 the proportional resampling method was chosen for use in this study. Furthermore, the non-impervious surfaces consisted of many land-cover types (water, vegetation, cropland and bare area). As the bare land was easier to be confused with the impervious surface compared with the water and vegetation types especially in the cities with rapid urbanization (Weng, 2012), and the suburban areas or rural villages were also easy to confused with croplands (Li et al., 2015), the non-impervious surfaces were spited into three independent groups including: bare area, cropland and other land-cover types. Then, in order to guarantee

250 the rationality of training samples, the stratified random sampling strategy was applied at every 5°×5° geographical grids. Finally, the approximate value of 1:3 was used to represent the proportion of impervious to non-impervious surfaces (bare area, cropland and other land-cover types). Using the proportional resampling method and the stratified random sampling strategy, a total of 4,483,000 training samples, including 3,499,000 non-impervious samples and 984,000 impervious samples, were collected over the land areas across the globe.

Earth System
Science Data
Open Access
Discussions

3.2 Multi-source and multi-temporal impervious classification method

3.2.1 Multi-source and multi-temporal feature selection

As mentioned above, the datasets used in this study had been acquired from various satellite sensors and had distinctive features. Also the incorporation of multi-source and multi-temporal remote sensing data has been demonstrated to improve the accuracy of the mapping of impervious surfaces. In this study, three kinds of satellite imagery, including Landsat-8 SR, Sentinel-1 SAR and SRTM/ASTER DEM imagery, were collected for the global classification of impervious surfaces.

After masking out the bad pixels (cloud, shadow and saturated pixels), the time-series Landsat SR imagery were needed to reduce the number of dimensions of the temporal−spectral features to guard against the Hughes phenomenon (Zhang et al., 2019). Similar to what Hansen et al. (2014) and Zhang and Roy (2017) introduced to capture phenology, the 15th and 85th percentiles of Landsat SR were used instead of the minimum and maximum values to minimize the effects of residual shadows and cloud caused by the errors in the CFMask method (Massey et al., 2018). In addition, as the Sun et al. (2017) explained that the growing season was the best time for impervious surface mapping over temperate continental climate zones and Zhang et al. (2014a) found that winter (dry season) is the best season to estimate impervious surface in subtropical monsoon regions, the combination of 15th and 85th percentiles of Landsat SR was used to efficiently capture intra-annual variation information of various land-cover types. It should be noted that only the six optical bands (Blue, Green, Red, NIR, SWIR1 and SWIR2) were selected because the Coastal band was sensitive to the atmospheric scattering (Wang et al., 2016). Liu et al. (2018) found that the Normalized Difference Water Index (NDWI), Normalized Difference Vegetation Index (NDVI) and Normalized Difference Built-up Index (NDBI) were of great help in impervious surface identification; therefore, these three spectral indexes were added to the spectral features, giving a total of 18 features for the two-epoch imagery. Furthermore, as the texture information contributed to the classification performance (Weng, 2012), the local textural measures based on the Gray Level Co-occurrence Matrix (GLCM) were adopted; however, because of the redundancy and similarity between texture features (Rodriguez-Galiano et al., 2012), only the variance, dissimilarity and entropy of the NIR band were selected from the 7×7 local window for the two-epoch imagery (Chen et al., 2016; Zhang et al., 2014b). The optimal window size for texture measurements was highly dependent on the image spatial resolution and the land cover characteristics (Zhu et al., 2012) and Shaban and Dikshit (2001) computed texture measurements with different window sizes as inputs for urban area classification and suggested window sizes of 7 ×7 pixels perform best.

As the Sentinel-1 SAR imagery had been pre-processed in the GEE platform, the annual mean and standard deviation of the VV and VH imagery were directly derived from the time-series of Sentinel-1 SAR imagery. Zhang et al. (2014b) found that SAR texture features were also relevant to impervious surfaces and the dissimilarity, variance and entropy features of the VV and VH imagery were identified as effective indicators for the texture description of different urban land cover types. As Zhang et al. (2014b) explained the window size for calculating GLCM should be smaller as terrains are smaller under coarser resolution, the window size was chose as 9×9 pixels at 10-m spatial resolution, equivalent to 3×3 pixels in 30-m. Moreover,

as the spatial resolution of the Landsat SR (30-m) was three times that of the Sentinel-1 imagery (10-m), the SAR data were resampled to 30-m for integration with the Landsat SR data.

Lastly, as Clarke et al. (1997) found that terrain variables were of great help in identifying impervious surfaces, the elevation, slope and aspect, calculated from the SRTM/ASTER DEM data, were added to the feature vector. This gave a total of 37 features for each pixel location, including 18 spectral features and 6 texture features from the Landsat imagery, 10 SAR features and 3 topographical variables. The features are listed in Table 1.

Table 1. Training features for global impervious surface mapping.

Data	Features	References
LandSat-8 OLI	Reflectance: Blue, Green, Red, NIR, SWIR1 and SWIR2	Liu et al. (2018)
	Normalized indices: NDVI, NDWI and NDBI	
	Textural variables: variance, dissimilarity and entropy of the NIR	Chen et al. (2016)
Sentinel-1 SAR	Annual statistics: mean and standard deviation of VV and VH	Sun et al. (2019b)
	Textural features: dissimilarity, variance and entropy of VV and VH	Zhang et al. (2014b)
DEM	Elevation, slope and aspect	Clarke et al. (1997)

3.2.2 Random forest classification model

As in the work of Zhang and Roy (2017), there were two options for models to use in the global impervious surface classification: global and local models. The global model is a single classifier, trained using the global training samples, and then used to classify the entire global data set. The local model, is trained using regional samples; the regional classification results are then mosaicked to produce the global map. Zhang and Roy (2017) confirmed that locally adaptive models achieve a higher classification accuracy than a single global model. Therefore, the global land surfaces were split into approximately 1000 5°×5° geographical grid cells after considering the data volume and amount of computation needed for the regional mapping. In addition, to ensure the classification consistency across the cell boundaries, as in the work of Zhang et al. (2018c) and Zhang and Roy (2017), the training samples from the adjacent 3×3 geographical cells were also imported to train the classifier in classifying the central geographical cell.

As for the specific techniques used in classifiers, according to our previous investigations (Zhang et al., 2019), the Random Forest (RF) classifier is more capable of handling high-dimensional multicollinearity data. It is also less affected by noise and feature selection as well as being more accurate and efficient than other widely used classifiers such as the SVM (Support Vector Machine), CART (Classification And Regression Tree) and ANN (Artificial Neural Network) classifiers. Therefore, the RF classifier was selected for the development of the global impervious surface map.

The RF classifier has only two parameters: the number of classification trees (Ntree) and the number of selected predication features (Mtry). Furthermore, many researchers have demonstrated that there is almost no correlation between these two

parameters and the classification accuracy (Belgiu and Drăguţ, 2016; Du et al., 2015; Gislason et al., 2006); therefore, the default values of 500 for Ntree and the square root of the total number of training features for Mtry were selected.

3.3 Accuracy assessment

To quantitatively assess the global consistency between the MSMT_RF-based impervious surface map and the three existing
315   products (GlobeLand30-2010, FROM_GLC2015 and NUACI_2015), four global 30-m impervious surface maps were aggregated to a resolution of 0.05°×0.05° and the fraction of impervious area was then calculated. Following that, scatter plots of the linear regression between the MSMT_RF-based results and the reference data were produced to support the quantitative analysis. Two evaluation indicators − the coefficient of determination (R2) and the root mean square error (RMSE) − were calculated to measure the consistency.

320   In addition, a validation based on the visual interpretation samples was implemented over twelve 1°×1° regions covering different impervious surface densities and different continents. Four accuracy metrics, including the overall accuracy (O.A.), the producer's accuracy (P.A.), user's accuracy (U.A.) and kappa coefficient (Olofsson et al., 2014), were computed to assess the performance of the MSMT_RF-based global impervious surface mapping.

4 results

325   ### 4.1 Global impervious surface map and cross-comparison

The global distribution of the fraction of impervious area (FIA) at a spatial resolution of 0.05° is illustrated in Fig. 3, whilst the meridional and zonal total FIA for each 0.05° longitude and latitude bin are shown at the top and left of Fig. 3. From an intuitive and statistical perspective, globally, impervious surfaces are mainly concentrated in three continents: Asia (34.43%), North America (28.04%) and Europe (24.98%), followed by South America (5.89%), Africa (5.63%) and Australia (1.06%).

330   In addition, the zonal statistics indicate that 70% of the impervious surfaces are distributed between 30°N and 60°N because these regions contain the key areas of Asia, North America and Europe, which are the locations of the most developed countries and highest population densities. The meridional results illustrate that there are four peak intervals: 100° W to 70° W (United States), 10° W to 40° E (European Union), 60° E to 90° E (India) and 100° E to 130° E (China and southeastern Asia). The two peak values in the meridional direction are located in the centers of the United States and China.
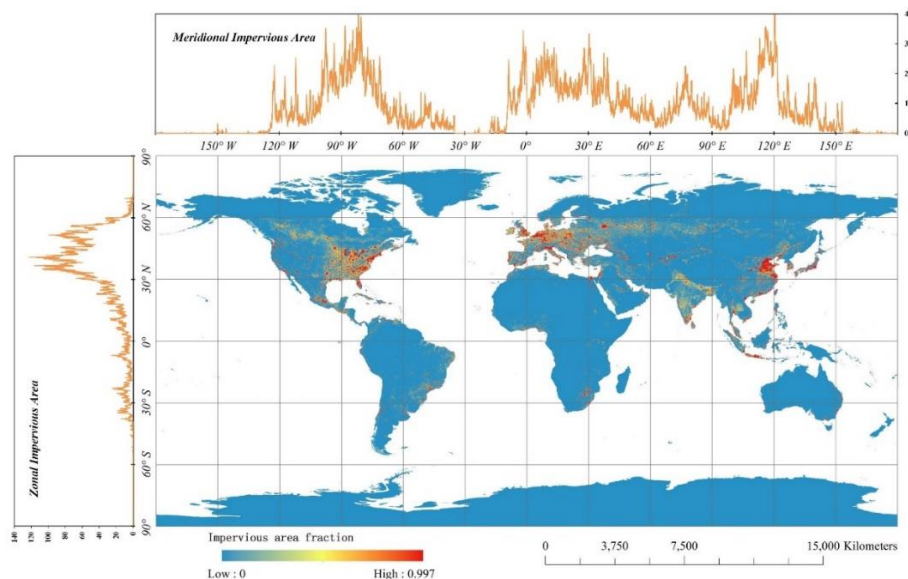
335

Figure 3. Global fraction of impervious cover derived from multi-source and multi-temporal Landsat-8 SR and Sentinel-1 SAR imagery acquired in 2015 to 2016. The spatial resolution of the map is 0.05°.

Summaries of the impervious surface areas at a national scale were also produced. The statistical results indicated that the total impervious surface areas of the top 20 countries account for 75.96% of the total global area. Fig. 4 presents the top 20 counties

340 in terms of impervious surface area and corresponding fractions of the world total. Overall, there is a positive correlation between these statistical fractions and the land area, population and degree of economic development of these nations. Specifically, it was found that the U.S. has the biggest impervious surface area, accounting for more than 20% of the global total, and only the top 3 countries (U.S., China and Russia) exceed 5% of the total global area. The ranking is also basically consistent with the statistics produced by the Organization for Economic Co-operation and Development (OECD) for built-up

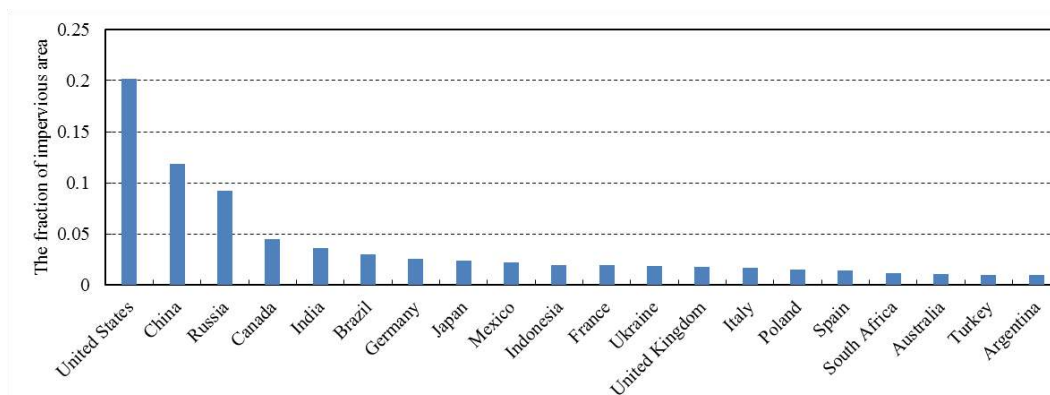345 areas in 2014 (https://stats.oecd.org/Index.aspx?DataSetCode=BUILT_UP).

Figure 4. The top 20 countries in terms of impervious surface area and corresponding fractions of the global total.

Earth System Science Data
Open Access Discussions

To quantitatively evaluate the consistency between the MSMT_RF-based impervious surface map and the three existing products (GlobeLand30-2010, FROM_FLC2015 and NUACI_2015), four global 30-m impervious surface maps were first

350 aggregated to a resolution of 0.05°. Scatter plots of the three products against the MSMT_RF-based impervious map were then made, as illustrated as Fig. 5. The results indicate that there is a greater consistency between the MSMT_RF-based map and FROM_GLC2015 (R2 of 0.7696 and RMSE of 0.0546), than for GlobeLand30-2010 (R2 of 0.7416 and RMSE of 0.0604) or NUACI_2015 (R2 of 0.6631 and RMSE of 0.0996). The main differences between the GlobeLand30 and the MSMT_RF-based maps are due to the temporal interval of 5 years and the limitations of the minimum 4×4 mapping unit for GlobeLand30-

355 2010 (Chen et al., 2015). As NUACI_2015 has been demonstrated to miss some small, fragmented villages and roads (Sun et al., 2019b), the slope of the regression line was less than 1.0 in this case. Lastly, subsequent validation (Section 4.2) indicated that there was a high degree of consistency (close to 1:1) between FROM_GLC2015 and the MSMT_RF-based results in high-density regions but that the product suffered from the problem of underestimation in low and medium-density regions. The slope of the regression line for these results is also less than 1.
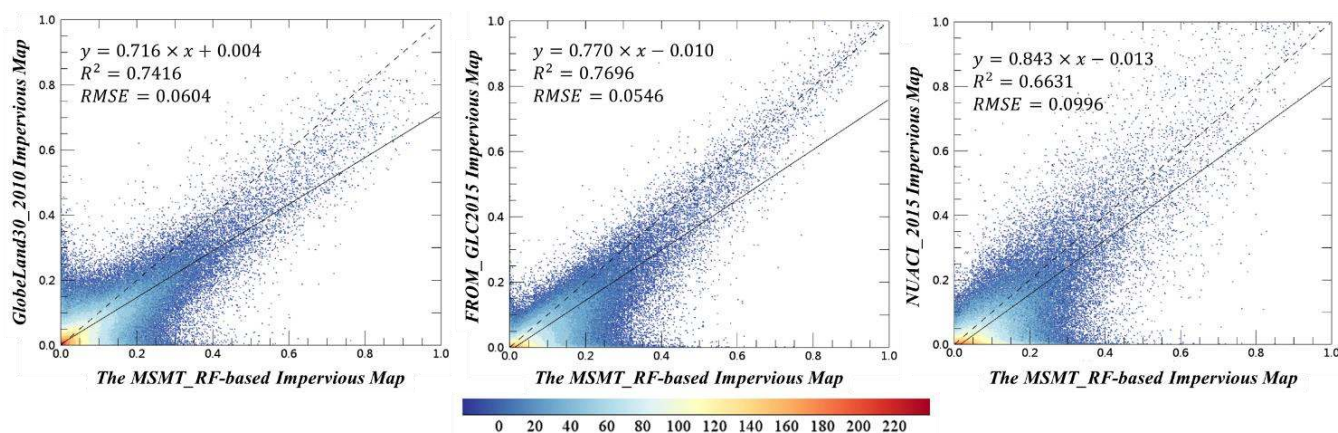
360

Figure 5. Scatter plots between the MSMT_RF-based impervious map and the GlobeLand30-2010, FROM_GLC2015 and NUACI_2015 global impervious surface products at a spatial resolution of 0.05°×0.05°.

4.2 Accuracy assessment using validation samples

The accuracy of the four global impervious surface maps over 12 validation regions with different impervious densities is

365 presented in Table 2. Six evaluation metrics, including the producer's accuracy (which measures the commission error) and user's accuracy (which measures the omission error) of the impervious surface, the producer's and user's accuracy of non-impervious surfaces as well as the overall accuracy and kappa coefficient, were used to assess the accuracy. Overall, the MSMT_RF-based map achieved the highest overall accuracy of 0.966 and kappa coefficient of 0.903 compared with 0.925 and 0.769 for FROM_GLC2015, 0.873 and 0.585 for NUACI_2015, and 0.911 and 0.717 for GlobeLand30-2010 using all 12

370 regional validation data. From the perspective of the value of the producer's accuracy for impervious surfaces, the MSMT_RF method performed significantly better than the other impervious surface products, especially in the low- and medium-density

14

regions. Specifically, as the minimum mapping unit of GlobeLand30 was a 4×4-pixel area, many rural impervious surfaces were ignored in these low and medium-density regions, which caused large omission errors that ranged from 73.6% to 12.4%. NUACI_2015 had the lowest producer's accuracy and this might be due to its poor performance over small impervious surfaces

375   (Sun et al., 2019b). FROM_GLC2015 had a similar performance to the MSMT_RF method for high-density regions, but its accuracy decreased sharply over low- and medium-density regions. Moreover, we could found that the producer's accuracy for impervious surfaces and kappa coefficient varied with the impervious density, specifically, the higher accuracies were achieved at high impervious density regions followed by medium and low impervious density regions. As the stratified random sampling strategy was applied to each validation region independently, the low and medium density regions were easier to

380   select these mixed impervious validation points (simultaneously containing the impervious and non-impervious surfaces in the 30-m ×30-m validation window and the impervious areas exceed the predefined threshold of 50%) which were most difficult to identify for impervious surface mapping.

As for the user's accuracy for impervious surfaces, and the producer's accuracy and user's accuracy for non-impervious surfaces, the MSMT_RF method achieved an accuracy similar to that achieved by FROM_GLC2015 and GlobeLand30-2010

385   and higher than that of NUACI_2015. In contrast to the results for the producer's accuracy for impervious surfaces, the three other products mostly performed very well as measured by these three metrics, especially in low- and medium-density regions.

Table 2. Accuracy of the four impervious surface maps over 12 validation regions

		a	b	c	d	e	f	g	h	i	J	k	l	Overall
	I.D.	high	low	low	high	medium	medium	low	high	high	medium	high	medium	
The MSMT_RF map	**P.I.**	**0.885**	**0.822**	**0.847**	**0.938**	**0.757**	**0.782**	**0.765**	**0.905**	**0.990**	**0.941**	**0.969**	**0.845**	0. 900
	U.I.	0.955	0.961	1.000	0.944	0.858	0.991	1.000	0.987	0.940	0.923	0.948	0.990	0.952
	P.N.	0.979	0.994	1.000	0.971	0.974	0.999	1.000	0.996	0.985	0.980	0.962	0.999	0.986
	U.N.	0.944	0.969	0.975	0.969	0.951	0.958	0.965	0.970	0.998	0.985	0.977	0.974	0.970
	O.A.	0.948	0.968	0.978	0.968	0.937	0.960	0.968	0.974	0.986	0.972	0.965	0.976	0.966
	Kappa	**0.880**	**0.868**	**0.905**	**0.910**	**0.767**	**0.852**	**0.850**	**0.927**	**0.955**	**0.914**	**0.928**	**0.898**	0.903
FROM_GLC2015	**P.I.**	**0.965**	**0.100**	**0.824**	**0.787**	**0.272**	**0.489**	**0.395**	**0.819**	**0.974**	**0.525**	**0.942**	**0.112**	0. 715
	U.I.	0.910	0.900	1.000	0.967	0.925	1.000	1.000	0.939	0.873	0.991	0.980	1.000	0.948
	P.N.	0.955	0.998	1.000	0.986	0.996	1.000	1.000	0.983	0.966	0.999	0.986	1.000	0.988
	U.N.	0.983	0.862	0.972	0.900	0.869	0.907	0.914	0.944	0.994	0.891	0.959	0.869	0.920
	O.A.	0.958	0.862	0.975	0.919	0.872	0.915	0.918	0.943	0.968	0.901	0.968	0.871	0.925
	Kappa	**0.906**	**0.155**	**0.889**	**0.810**	**0.372**	**0.615**	**0.531**	**0.838**	**0.900**	**0.634**	**0.933**	**0.178**	0.769
NUACI_2015	**P.I.**	**0.309**	**0.211**	**0.141**	**0.680**	**0.162**	**0.579**	**0.247**	**0.626**	**0.758**	**0.539**	**0.843**	**0.042**	0. 527
	U.I.	0.669	1.000	1.000	0.871	0.786	0.939	0.952	0.788	0.900	1.000	0.933	0.556	0.873
	P.N.	0.928	1.000	1.000	0.948	0.991	0.993	0.998	0.946	0.980	1.000	0.957	0.994	0.977
	U.N.	0.741	0.877	0.876	0.852	0.852	0.922	0.895	0.887	0.944	0.894	0.894	0.855	0.874
	O.A.	0.730	0.881	0.879	0.857	0.849	0.924	0.897	0.868	0.937	0.905	0.909	0.852	0.873
	Kappa	**0.277**	**0.312**	**0.220**	**0.664**	**0.223**	**0.675**	**0.356**	**0.614**	**0.785**	**0.650**	**0.811**	**0.058**	0.585
GlobeLand30-2010	**P.I.**	**0.876**	**0.244**	**0.671**	**0.500**	**0.346**	**0.263**	**0.593**	**0.774**	**0.895**	**0.642**	**0.785**	**0.310**	0. 641
	U.I.	0.926	1.000	1.000	0.944	0.904	1.000	1.000	0.940	0.971	0.985	0.982	1.000	0.960
	P.N.	0.967	1.000	1.000	0.985	0.992	1.000	1.000	0.984	0.994	0.997	0.990	1.000	0.992
	U.N.	0.943	0.882	0.949	0.793	0.881	0.872	0.940	0.931	0.975	0.915	0.865	0.895	0.902
	O.A.	0.938	0.886	0.953	0.820	0.882	0.878	0.945	0.933	0.975	0.925	0.904	0.900	0.911
	Kappa	**0.855**	**0.355**	**0.778**	**0.547**	**0.448**	**0.373**	**0.716**	**0.806**	**0.916**	**0.734**	**0.797**	**0.435**	0.717

390 Note: I.D., impervious density, P.I., producer's accuracy of impervious surfaces, U.I., user's accuracy of impervious surfaces, P.N.,

producer's accuracy of non-impervious surfaces, U.N., user's accuracy of non-impervious surfaces, O.A., overall accuracy.

To intuitively compare the performance of these four products, five validation regions, including two high-density regions,

one low-density and two medium-density regions, were selected in Figure 6. First, in the low-density region (Table 2b and

Figure 6b), FROM_GLC2015 had the most obvious underestimation problem, except for the urban centers, almost all
395   impervious objects (peripheral urban and rural villages and roads) were missed. The series omission error maybe came from
the sparse training samples (91,433 training samples in the globe) (Gong et al., 2013). The NUACI_2015, only identifying the
urban areas and some obvious impervious objects, also missed fragmented and small rural villages. The causes of omission
maybe came from the threshold method used by the NUACI_2015, specifically, Liu et al. (2018) developed a novel NUACI
index to enhance the impervious surfaces and suppress the non-impervious surfaces and then found an optimal threshold for
400   NUACI index to split the impervious and non-impervious surfaces. However, the NUACI values of rural villages and roads
were usually located in the mixed areas of impervious and non-impervious surfaces, so the NUACI_2015 had great ability for
obvious impervious surfaces but bad performance for fragmented impervious surfaces. As for the GlobeLand30-2010, the
omission errors were mainly due to the temporal interval of 5 years and the minimum 4×4 mapping unit(Chen et al., 2015).

Next, in the first high-density region (Table 2d), GlobeLand30-2010 produced underestimates in many peripheral urban areas,
405   which was mainly due to the temporal interval of 5 years. FROM_GLC2015 and NUACI_2015 still omitted some rural roads
and villages (top-right and center-left of Figure 6d) compared with the MSMT_RF-based results. In the second high-density
region (Table 2i), NUACI_2015 identified large and medium-sized cities at the cost of missing all of the fragmented villages.
The MSMT_RF-based results and FROM_GLC2015 accurately delineated the spatial distributions of urban and rural roads
and settlements. GlobeLand30-2010 still suffered from a few omission errors caused by the temporal difference between data
410   sets and the limitation of minimum mapping unit.

Lastly, in the first medium-density region (Table 2j and Fig. 6j), the situation was similar to that for Figure 6d − the omission
errors in FROM_GLC2015, NUACI_2015 and GlobeLand30-2010 were caused by the omission of small and fragmented
villages and roads. As for the last validation region, the medium-density region (Table 2l and Figure 6l) consisted of typical
rural areas of North America containing a large number of small and rural roads. As Figure 6l illustrates, almost all roads and
415   villages were missed in FROM_GLC2015 and NUACI_2015 whereas GlobeLand30-2010 could identify the main roads while
still missing the minor roads. In summary, as the MSMT_RF method could accurately and comprehensively identify
fragmented and small villages and roads, it gave a higher producer's accuracy.

17
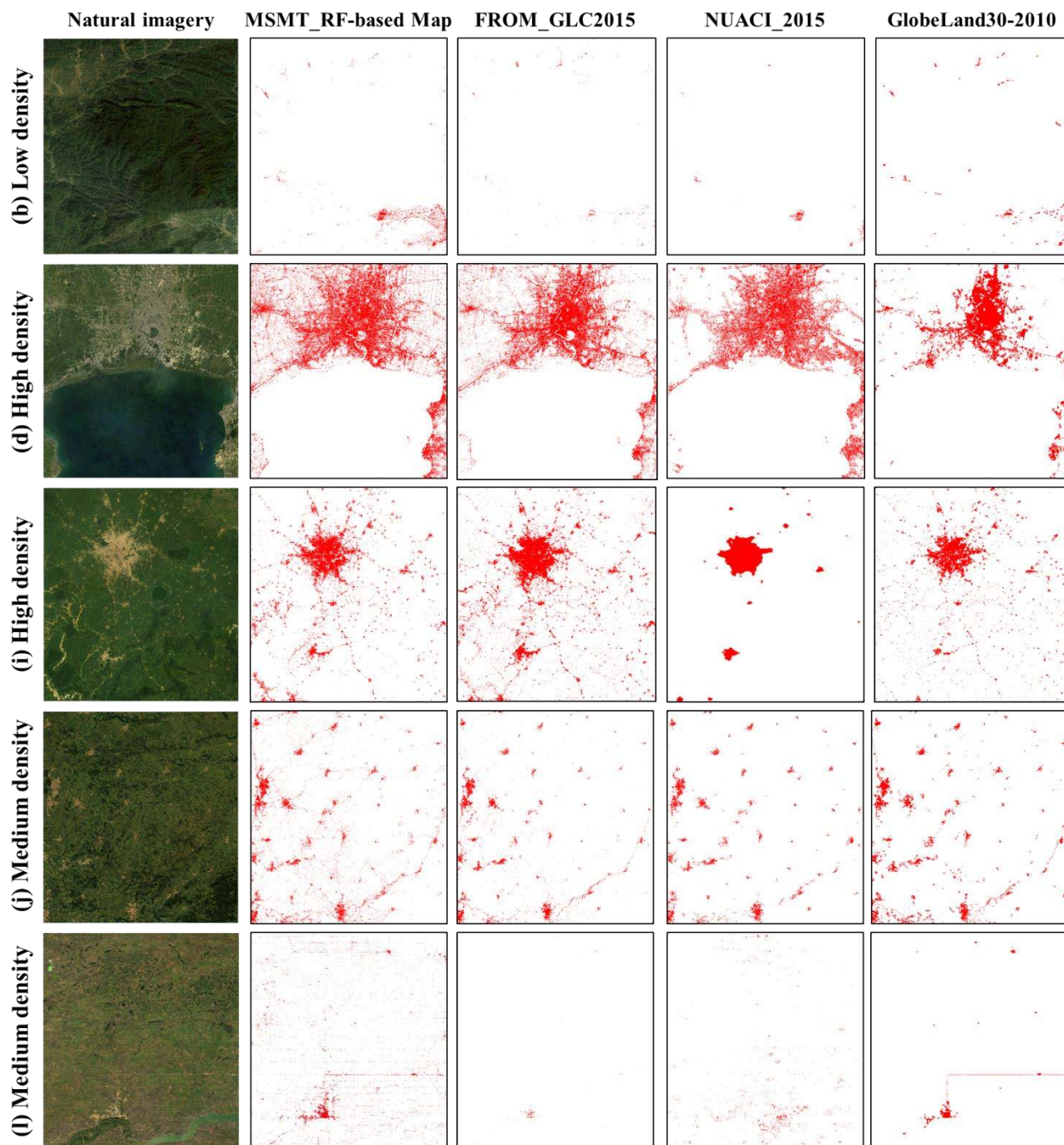
Figure 6. Comparisons between the MSMT_RF-based maps (the second column) and other impervious surface products (the 3rd to 5th columns corresponded to the FROM_GLC products developed by Gong et al. (2013), the NUACI products developed by Liu et al. (2018) and the GlobeLand30 products developed by Chen et al. (2015), respectively) for five regions with various impervious surface densities. The first column listed the corresponding natural-composited Landsat images in the growing season of 2015.

5 Discussion

5.1 The advantages of multi-source and multi-temporal classification

Because of the spectral heterogeneity of impervious surfaces, it is very difficult to accurately map impervious surfaces using only optical remote sensing imagery (Zhang et al., 2014b). Although some studies have demonstrated that the integration of multi-source and multi-temporal information can improve the mapping accuracy, these studies mainly focused on the regional scale and regions of high impervious surface density (Zhang et al., 2014b; Zhu et al., 2012). At present, global impervious surface maps are still produced by optical imagery alone or by using a combination of optical and DMSP-OLS or VIIRS NTL imagery (Huang et al., 2016; Liu et al., 2018; Schneider et al., 2010). In this study, we first developed the global 30-m impervious surface map using multi-source and multi-temporal imagery. To quantitatively demonstrate the need for using multi-source, multi-temporal information and the results of using it, we randomly selected six 5°×5° regions (red rectangles in Fig. 1) from six different continents and then calculated the importance of the training features using the RF model at the Python environment. Specifically, the RF model computed the average increase in the mean square error by permuting out-of-bag data for a variable while keeping all the other variables constant, thus measuring the variable's importance (Pflugmacher et al., 2014). Training features that had a high importance were the drivers of the model decision and their values had a significant impact on the output values.

The importance of all 37 training features for the six regions is illustrated in Fig. 7. These results indicate that the Sentinel-1 SAR features (VV and VH) had the greatest contribution to the final decision in most regions because SAR images can provide information about the structure and dielectric properties of the surface materials. Next in importance were the 15th percentile of Landsat SR in the blue, green, red and SWIR2 bands and the corresponding NDVI and NDWI indices, as well as the texture variance and dissimilarity for Sentinel-1 SAR: the importance of these feature was close to or exceeded 5% in most cases. Following these were the 85th percentile of Landsat SR in the NIR and SWIR1 bands as well as the SAR texture features, whose mean importance was approximately 3%. In summary, only the integration of multi-source training features could guarantee the classification accuracy across different impervious landscapes. Similarly, Zhang et al. (2014b) also concluded that the combination of optical and SAR imagery could significantly improve the land-cover classification and impervious surface area estimation.

Secondly, as the intra-annual variability could increase the separability of impervious and non-impervious surfaces (Zhang and Weng, 2016), the importance of multi-temporal optical features was also investigated. Although the 15th percentile had a higher importance than the 85th percentile in most of the spectral bands, we found that there was a large degree of complementarity between the images from two different seasons: for example, the importance of the 15th percentile in the NIR and SWIR1 bands was low while that of 85th percentile was high. Therefore, the total importance of the bi-seasonal spectral features exceeded 70% in some cases. Similarly, Zhu et al. (2012) demonstrated that the inclusion of multi-temporal imagery increased the accuracy by 8.9%. Schug et al. (2018) also found that bi-seasonal information could produce a more

Earth System
Science
Data

Open Access

Discussions

reliable performance than a single-year composited image. Therefore, temporal variability can be considered an important addition to accurate impervious surface mapping.

Lastly, although the importance of Landsat texture features and the topographical variables was lower than 5% in these six regions, some scientists have demonstrated that these features contribute a lot to the improvement of impervious mapping

460   accuracy. For example, Shaban and Dikshit (2001) found that the combination of texture and spectral features improved the classification accuracy by 9% to 17% compared with the use of pure spectral features. Zhu et al. (2012) also emphasized that the integration of texture variables increased the accuracy from 86.86% to 92.69% because texture imagery could capture the local spatial structure and the variability of land-cover categories. Subsequently, the cumulative importance of topographical variables over the region in Asia exceeded 5%, the topographical variables were necessary for impervious surface mapping in

465   mountain areas. Similarly, Clarke et al. (1997) explained that topographical variables (slope, aspect and DEM) contribute a lot to impervious surface mapping. These features are, therefore, indispensable in the accurate mapping of impervious surfaces in complex landscapes.
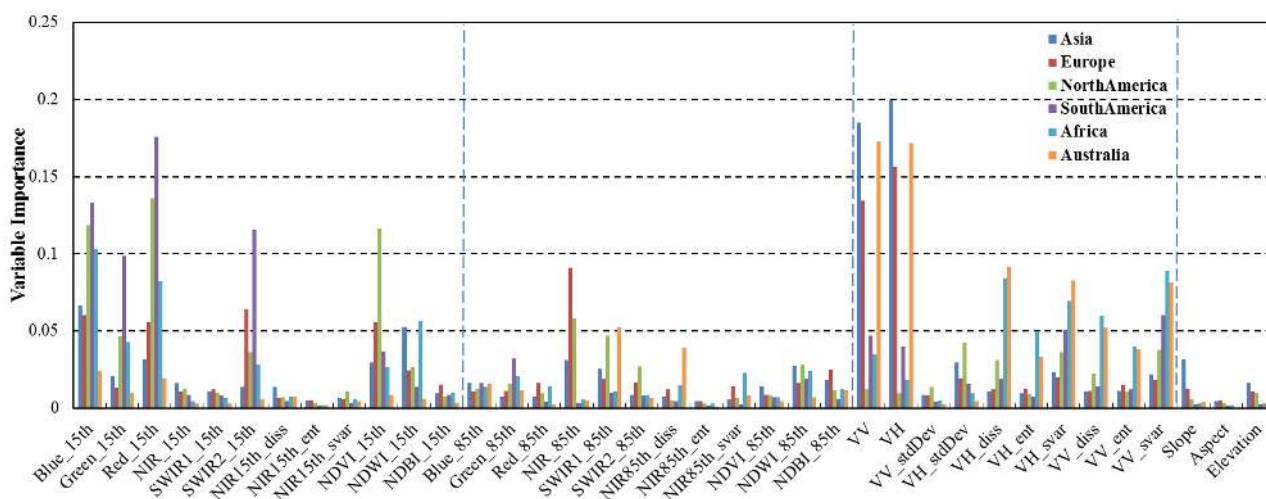
Figure 7. The importance of the input features derived from the random forest model using the training samples in six continental
470   **regions.**

From the perspective of the impervious mapping method, the comparison between our MSMT_RF product and NUACI_2015 also demonstrates that the classification-based method performed better than the spectral index-based method (Section 4.2). We concluded that this improvement was mainly due to the combination of the multi-source and multi-temporal information in the classification method.

5.2 Reliability and sensitivity of the global training samples

In contrast to other classification-related studies that require manual efforts to collect training samples (Gao et al., 2012; Im et al., 2012; Zhang et al., 2016), we overcame the expensive cost of collecting accurate and sufficient training samples at a global scale. To ensure the accuracy and reliability of the training samples, a combination of the GlobeLand30-2010 land-cover product, which had been validated to have a user's accuracy (which measures the commission error) of 97.1% for impervious surfaces (see Section 4.2), and DMSP-OLS NTL imagery was adopted to guarantee the reliability of each sample. As it was difficult and challenging to evaluate the accuracy of all the training samples, we randomly selected 1% of the total training samples (in Section 3.1) including 34,990 non-impervious and 9,840 impervious points to measure the reliability of the global training samples. After careful checking, we found that these training samples achieved accuracies of 91.9% and 99.5% for impervious and non-impervious surfaces, respectively.

Meanwhile, even if the training samples still contained a small number of erroneous points, the random forest model has been demonstrated to be resistant to noise and presence of erroneous samples (Belgiu and Drăguţ, 2016). In this study, we randomly changed the category of a certain percentage of the 34,990 samples and used the ''noisy'' samples to train the random forest classifier. Fig. 8 illustrates the overall accuracy and impervious producer's accuracy decreased for the increased percentage of erroneous samples. It was found that the overall and impervious producer's accuracy remained stable when the percentage of erroneous samples increased from 1% to 20% while it rapidly decreased when the percentage of erroneous samples was higher than 20%. Similarly, Gong et al. (2019) also found that the decrease in overall accuracy was less than 1% when the error in the training samples was less than 20%.
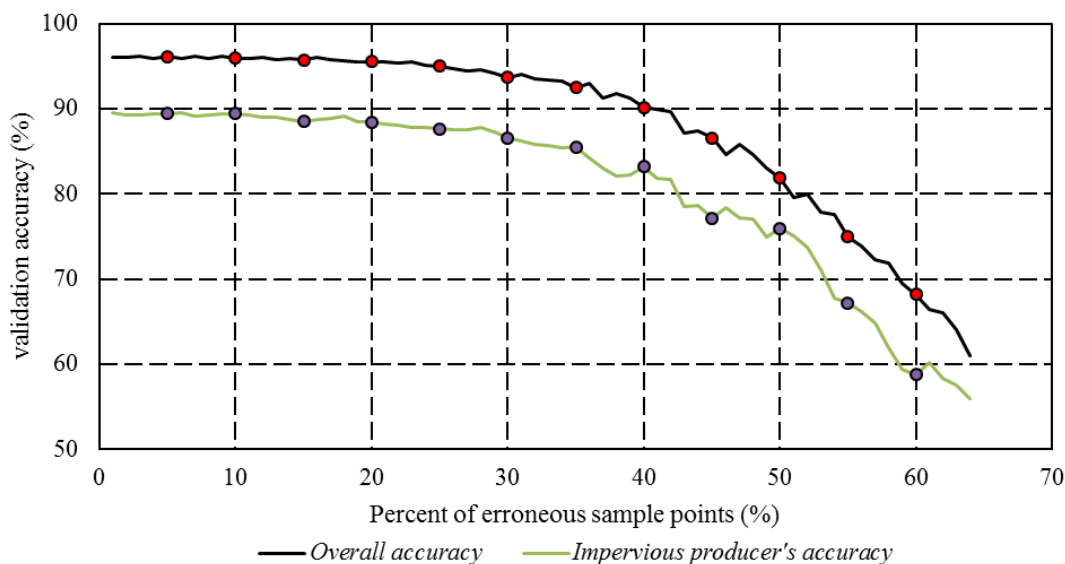

Figure 8. Sensitivity analysis showing the relation between the classification accuracy and the percentage of erroneous samples points.

Earth System
Science
Data

Open Access Discussions

495   Therefore, the reliability and sensitivity analysis indicated that: 1) the random forest model is resistant to noisy training samples
       and performs well if the percentage of erroneous samples is lower than 20%; and 2) the training samples derived from the
       GlobeLand30 and DMSP-OLS NTL imagery were accurate enough for use in global impervious surface mapping.

5.3 Limitations of the proposed method

       Although the proposed MSMT_RF method has been demonstrated to have the ability to produce the accurate impervious
500   surface products, there are still some limitations to the method. First, as the training samples derived from the GlobeLand30-
       2010 are restricted to a 9×9-pixel local window and further refined by the integration of MODIS EVI and VIIRS NTL imagery,
       low-density impervious samples might be omitted and cause further omission of low-density impervious surfaces (rural
       villages, small roads and so on). Although, in this study, spatially adjacent training samples from the surrounding 3×3 areas
       were imported to reduce the omission of low-density samples, according to the accuracy assessment, higher omission errors
505   were found in low and medium-density regions than in high-density regions. Therefore, our future work will pay more attention
       to the omission of low-density impervious surfaces.

       Secondly, as Weng (2012) pointed out, mixed pixels are common in medium-resolution imagery due to the limitations of the
       spatial resolution and spectral heterogeneity of the landscape. The effectiveness of 'hard' classifiers is easily affected by these
       mixed pixels (low-density impervious pixels also constitute mixed pixels). Due to the proportion of impervious surfaces within
510   a pixel, impervious surface areas are often overestimated in urban areas or underestimated in rural areas when using medium-
       resolution images (Lu and Weng, 2006). Therefore, our future work will focus on simultaneously producing the likelihood
       ('soft' probability) of each pixel being an impervious surface. At present, some scientists have produced continuous impervious
       fractions at a regional scale: for example, Okujeni et al. (2018) used the support vector regression method to estimate the
       fraction of impervious surfaces at the pixel scale.

6 Data availability and user guidelines

515

       The global impervious surface map data set generated in this paper are available on Zenodo:
       https://doi.org/10.5281/zenodo.3505079 (Zhang and Liu, 2019).

       To facilitate the readers to reproduce this work, Table 3 gives the details of the datasource and platform information of the
       datasets and processes in this study. The input remote sensing datasets and products came from three parts including: GEE
520   platform, free access websites and our group. Specifically, five kinds of basic datasets in section 2.1 were available at GEE
       platform. The three global impervious surface products in section 2.2 were downloaded from the free access websites from
       National Geomatics Center of China, Tsinghua University and Sun Yat-sen University. The validation samples were produced
       by our group using visual interpretation.

       Further, the process of derivation of global training samples was implemented by using the multi-source datasets at localhost
525   computation platform, and the random forest classification at each 5°×5° regional grid was developed by our group on the

GEE platform using JavaScript language. The importance of multi-source and multi-temporal features and reliability and sensitivity of global training samples were analyzed at the localhost Python computation environment.

Table 3. The detailed information of the datasets and processes in this study

	Datasource and platform	Detailed datasets and processing steps
Datasets	Google Earth Engine platform	Landsat-8 optical, Sentinel-1 SAR, VIIRS NTL, MODIS EVI and STRM/ASTER DEM topographical imagery
	Free download websites	GlobeLand30-2010, FROM_GLC-2015, NUACI-2015 products
	Our Group	Validation samples
Processes	Google Earth Engine platform (JavaScript language)	The random forest classification at each 5°×5° regional grid
	Localhost platform (Python environment)	Derivation of global training samples The importance of multi-source and multi-temporal features reliability and sensitivity of global training samples

7 Conclusions

530　Due to the spectral heterogeneity and complicated make-up of impervious surfaces, large-area impervious mapping is challenging and difficult. In this study, a global 30-m impervious surface map was developed by using multi-source, multi-temporal remote sensing data based on the Google Earth Engine platform. First, the global training samples were automatically derived from the GlobeLand30-2010 land-cover product together with VIIRS NTL and MODIS EVI imagery. Then, a local adaptive random forest model was trained using the training samples and multi-source and multi-temporal datasets for each

535　5°×5° geographical grid. Following that, the global impervious map produced by mosaicking a large number of 5°×5° regional impervious surface maps was validated by comparing it with three existing products (GlobeLand30-2010, FROM_GLC2015 and NUACI_2015) using approximately 10,142 interpretation samples. The results indicated that the MSMT_RF-based impervious surface map had the highest overall accuracy of 96.7% and a kappa coefficient of 0.888, followed by FROM_GLC2015 (92.5% and 0.769), GlobeLand30-2010 (91.1% and 0.717) and NUACI_2015 (87.43% and 0.585).

540　Therefore, it can be concluded that the global 30-m impervious surface map produced by the proposed MSMT_RF method is accurate and reliable for use in global impervious surface mapping.

Author contributions. Conceptualization, Liangyun Liu; Investigation, Xiao Zhang; Methodology, Liangyun Liu and Xiao Zhang; Software, Xiao Zhang and Xidong Chen; Validation, Xiao Zhang, Shuai Xie, Xidong Chen and Yuan Gao; Writing – original draft preparation, Xiao Zhang; writing—review and editing, Shuai Xie, Bing Zhang and Changshan Wu.

545　**Competing interests.** The authors declare that they have no conflict of interest.

References

Bai, Y., Feng, M., Jiang, H., Wang, J., and Liu, Y.: Validation of Land Cover Maps in China Using a Sampling-Based Labeling Approach,
Remote Sensing, 7, 10589-10606, https://doi.org/10.3390/rs70810589, 2015.
555 Belgiu, M. and Drăguţ, L.: Random forest in remote sensing: A review of applications and future directions, ISPRS Journal of
Photogrammetry and Remote Sensing, 114, 24-31, https://doi.org/10.1016/j.isprsjprs.2016.01.011, 2016.
Bennett, M. M. and Smith, L. C.: Advances in using multitemporal night-time lights satellite imagery to detect, estimate, and monitor
socioeconomic dynamics, Remote Sensing of Environment, 192, 176-197, https://doi.org/10.1016/j.rse.2017.01.005, 2017.
Berger, M., Moreno, J., Johannessen, J. A., Levelt, P. F., and Hanssen, R. F.: ESA's sentinel missions in support of Earth system science,
560 Remote Sensing of Environment, 120, 84-90, https://doi.org/10.1016/j.rse.2011.07.023, 2012.
Chen, J., Chen, J., Liao, A., Cao, X., Chen, L., Chen, X., He, C., Han, G., Peng, S., Lu, M., Zhang, W., Tong, X., and Mills, J.: Global land
cover mapping at 30m resolution: A POK-based operational approach, ISPRS Journal of Photogrammetry and Remote Sensing, 103, 7-27,
https://doi.org/10.1016/j.isprsjprs.2014.09.002, 2015.
Chen, X., Cao, X., Liao, A., Chen, L., Peng, S., Lu, M., Chen, J., Zhang, W., Zhang, H., and Han, G.: Global mapping of artificial surfaces
565 at 30-m resolution, Science China Earth Sciences, 59, 2295-2306, https://doi.org/10.1007/s11430-016-5291-y, 2016.
Clarke, K. C., Hoppen, S., and Gaydos, L.: A self-modifying cellular automaton model of historical urbanization in the San Francisco Bay
area, Environment and planning B: Planning and design, 24, 247-261, https://doi.org/10.1068/b240247, 1997.
Deng, C. and Wu, C.: BCI: A biophysical composition index for remote sensing of urban environments, Remote Sensing of Environment,
127, 247-259, https://doi.org/10.1016/j.rse.2012.09.009, 2012.
570 Didan, K., Munoz, A. B., Solano, R., and Huete, A.: MODIS vegetation index user's guide (MOD13 series), Vegetation Index and Phenology
Lab, The University of Arizona. , doi: 10.5067/MODIS/MYD13Q1.006, 2015. 1-38, https://doi.org/10.5067/MODIS/MYD13Q1.006, 2015.
Du, P., Samat, A., Waske, B., Liu, S., and Li, Z.: Random Forest and Rotation Forest for fully polarized SAR image classification using
polarimetric and spatial features, Isprs Journal of Photogrammetry & Remote Sensing, 105, 38-53,
https://doi.org/10.1016/j.isprsjprs.2015.03.002, 2015.
575 Elvidge, C. D., Baugh, K., Zhizhin, M., Feng, C. H., and Ghosh, T.: VIIRS night-time lights, International Journal of Remote Sensing, doi:
10.1080/01431161.2017.1342050, 2017. 1-20, https://doi.org/10.1080/01431161.2017.1342050, 2017.
Elvidge, C. D., Tuttle, B. T., Sutton, P. C., Baugh, K. E., Howard, A. T., Milesi, C., Bhaduri, B. L., and Nemani, R.: Global Distribution and
Density of Constructed Impervious Surfaces, Sensors, 7, 1962-1979, https://doi.org/10.3390/s7091962, 2007.
ESA: Sentinel-1 SAR User Guide Introduction. Availabe online: https://sentinel.esa.int/web/sentinel/user-guides/sentinel-1-sar (accessed on
580 26 December 2019), 2016.
Farr, T. G., Rosen, P. A., Caro, E., Crippen, R., Duren, R., Hensley, S., Kobrick, M., Paller, M., Rodriguez, E., Roth, L., Seal, D., Shaffer,
S., Shimada, J., Umland, J., Werner, M., Oskin, M., Burbank, D., and Alsdorf, D.: The Shuttle Radar Topography Mission, Reviews of
Geophysics, 45, https://doi.org/10.1029/2005rg000183, 2007.
Foody, G. M. and Mathur, A.: Toward intelligent training of supervised image classifications: directing training data acquisition for SVM
585 classification, Remote Sensing of Environment, 93, 107-117, https://doi.org/10.1016/j.rse.2004.06.017, 2004.
Fu, P. and Weng, Q.: A time series analysis of urbanization induced land use and land cover change and its impact on land surface temperature
with Landsat imagery, Remote Sensing of Environment, 175, 205-214, https://doi.org/10.1016/j.rse.2015.12.040, 2016.
Gao, F., Colstoun, E. B. d., Ma, R., Weng, Q., Masek, J. G., Chen, J., Pan, Y., and Song, C.: Mapping impervious surface expansion using
medium-resolution satellite image time series: a case study in the Yangtze River Delta, China, International Journal of Remote Sensing, 33,
590 7609-7628, https://doi.org/10.1080/01431161.2012.700424, 2012.
Gislason, P. O., Benediktsson, J. A., and Sveinsson, J. R.: Random Forests for land cover classification, Pattern Recognition Letters, 27,
294-300, https://doi.org/10.1016/j.patrec.2005.08.011, 2006.
Goldblatt, R., Stuhlmacher, M. F., Tellman, B., Clinton, N., Hanson, G., Georgescu, M., Wang, C., Serrano-Candela, F., Khandelwal, A. K.,
Cheng, W.-H., and Balling, R. C.: Using Landsat and nighttime lights for supervised pixel-based image classification of urban land cover,
595 Remote Sensing of Environment, 205, 253-275, https://doi.org/10.1016/j.rse.2017.11.026, 2018.
Gong, P., Liu, H., Zhang, M., Li, C., Wang, J., Huang, H., Clinton, N., Ji, L., Li, W., Bai, Y., Chen, B., Xu, B., Zhu, Z., Yuan, C., Ping Suen,
H., Guo, J., Xu, N., Li, W., Zhao, Y., Yang, J., Yu, C., Wang, X., Fu, H., Yu, L., Dronova, I., Hui, F., Cheng, X., Shi, X., Xiao, F., Liu, Q.,
and Song, L.: Stable classification with limited sample: transferring a 30-m resolution sample set collected in 2015 to mapping 10-m
resolution global land cover in 2017, Science Bulletin, doi: 10.1016/j.scib.2019.03.002, 2019. https://doi.org/10.1016/j.scib.2019.03.002,
600 2019.

Gong, P., Wang, J., Yu, L., Zhao, Y., Zhao, Y., Liang, L., Niu, Z., Huang, X., Fu, H., Liu, S., Li, C., Li, X., Fu, W., Liu, C., Xu, Y., Wang, X., Cheng, Q., Hu, L., Yao, W., Zhang, H., Zhu, P., Zhao, Z., Zhang, H., Zheng, Y., Ji, L., Zhang, Y., Chen, H., Yan, A., Guo, J., Yu, L., Wang, L., Liu, X., Shi, T., Zhu, M., Chen, Y., Yang, G., Tang, P., Xu, B., Giri, C., Clinton, N., Zhu, Z., Chen, J., and Chen, J.: Finer resolution observation and monitoring of global land cover: first mapping results with Landsat TM and ETM+ data, International Journal of

605 Remote Sensing, 34, 2607-2654, https://doi.org/10.1080/01431161.2012.748992, 2013.

Gorelick, N., Hancher, M., Dixon, M., Ilyushchenko, S., Thau, D., and Moore, R.: Google Earth Engine: Planetary-scale geospatial analysis for everyone, Remote Sensing of Environment, 202, 18-27, https://doi.org/10.1016/j.rse.2017.06.031, 2017.

Guide, P.: Landsat 8 surface reflectance code (LaSRC) product, Availabe online: https://landsat.usgs.gov/sites/default/files/documents/lasrc_product_guide. pdf (accessed on 26 December 2018), 2018. 2018.

610 Hansen, M. C., Egorov, A., Potapov, P. V., Stehman, S. V., Tyukavina, A., Turubanova, S. A., Roy, D. P., Goetz, S. J., Loveland, T. R., Ju, J., Kommareddy, A., Kovalskyy, V., Forsyth, C., and Bents, T.: Monitoring conterminous United States (CONUS) land cover change with Web-Enabled Landsat Data (WELD), Remote Sensing of Environment, 140, 466-484, https://doi.org/10.1016/j.rse.2013.08.014, 2014.

Homer, C., Dewitz, J., Yang, L., Jin, S., Danielson, P., Xian, G., Coulston, J., Herold, N., Wickham, J., and Megown, K.: Completion of the 2011 national land cover database for the conterminous United States – Representing a decade of land cover change information,

615 Photogrammetric Engineering & Remote Sensing, 81, 345-354, https://doi.org/10.1016/S0099-1112(15)30100-2, 2015.

Homer, C., Huang, C., Yang, L., Wylie, B., and Coan, M.: Development of a 2001 national land-cover database for the United States, Photogrammetric Engineering & Remote Sensing, 70, 829-840, https://doi.org/10.14358/PERS.70.7.829, 2004.

Hu, Y., Liu, L., Liu, L., Peng, D., Jiao, Q., and Zhang, H.: A Landsat-5 atmospheric correction based on MODIS atmosphere products and 6S model, IEEE Journal of Selected Topics In Applied Earth Observations And Remote Sensing, 7, 1609-1615,

620 https://doi.org/10.1109/JSTARS.2013.2290028, 2014.

Huang, X., Schneider, A., and Friedl, M. A.: Mapping sub-pixel urban expansion in China using MODIS and DMSP/OLS nighttime lights, Remote Sensing of Environment, 175, 92-108, https://doi.org/10.1016/j.rse.2015.12.042, 2016.

Im, J., Lu, Z., Rhee, J., and Quackenbush, L. J.: Impervious surface quantification using a synthesis of artificial immune networks and decision/regression trees from multi-sensor data, Remote Sensing of Environment, 117, 102-113, https://doi.org/10.1016/j.rse.2011.06.024,

625 2012.

Jin, H., Stehman, S. V., and Mountrakis, G.: Assessing the impact of training sample selection on accuracy of an urban classification: a case study in Denver, Colorado, International Journal of Remote Sensing, 35, 2067-2081, https://doi.org/10.1080/01431161.2014.885152, 2014.

Jokar Arsanjani, J., Tayyebi, A., and Vaz, E.: GlobeLand30 as an alternative fine-scale global land cover map: Challenges, possibilities, and implications for developing countries, Habitat International, 55, 25-31, https://doi.org/10.1016/j.habitatint.2016.02.003, 2016.

630 Li, C., Peng, G., Wang, J., Zhu, Z., Biging, G. S., Yuan, C., Hu, T., Zhang, H., Wang, Q., and Li, X.: The first all-season sample set for mapping global land cover with Landsat-8 data, Science Bulletin, 62, 508-515, https://doi.org/10.1016/j.scib.2017.03.011, 2017.

Li, X., Gong, P., and Liang, L.: A 30-year (1984–2013) record of annual urban dynamics of Beijing City derived from Landsat data, Remote Sensing of Environment, 166, 78-90, https://doi.org/10.1016/j.rse.2015.06.007, 2015.

Li, X. and Zhou, Y.: Urban mapping using DMSP/OLS stable night-time light: a review, International Journal of Remote Sensing, 38, 6030-

635 6046, https://doi.org/10.1080/01431161.2016.1274451, 2017.

Li, X., Zhou, Y., Zhu, Z., Liang, L., Yu, B., and Cao, W.: Mapping annual urban dynamics (1985–2015) using time series of Landsat data, Remote Sensing of Environment, 216, 674-683, https://doi.org/10.1016/j.rse.2018.07.030, 2018.

Liu, X., Hu, G., Chen, Y., Li, X., Xu, X., Li, S., Pei, F., and Wang, S.: High-resolution multi-temporal mapping of global urban land using Landsat images based on the Google Earth Engine Platform, Remote Sensing of Environment, 209, 227-239,

640 https://doi.org/10.1016/j.rse.2018.02.055, 2018.

Lu, D. and Weng, Q.: Use of impervious surface in urban land-use classification, Remote Sensing of Environment, 102, 146-160, https://doi.org/10.1016/j.rse.2006.02.010, 2006.

Massey, R., Sankey, T. T., Yadav, K., Congalton, R. G., and Tilton, J. C.: Integrating cloud-based workflows in continental-scale cropland extent classification, Remote Sensing of Environment, 219, 162-179, https://doi.org/10.1016/j.rse.2018.10.013, 2018.

645 Okujeni, A., Canters, F., Cooper, S. D., Degerickx, J., Heiden, U., Hostert, P., Priem, F., Roberts, D. A., Somers, B., and van der Linden, S.: Generalizing machine learning regression models using multi-site spectral libraries for mapping vegetation-impervious-soil fractions across multiple cities, Remote Sensing of Environment, 216, 482-496, https://doi.org/10.1016/j.rse.2018.07.011, 2018.

Okujeni, A., van der Linden, S., Tits, L., Somers, B., and Hostert, P.: Support vector regression and synthetically mixed training data for quantifying urban land cover, Remote Sensing of Environment, 137, 184-197, https://doi.org/10.1016/j.rse.2013.06.007, 2013.

650 Olofsson, P., Foody, G. M., Herold, M., Stehman, S. V., Woodcock, C. E., and Wulder, M. A.: Good practices for estimating area and assessing accuracy of land change, Remote Sensing of Environment, 148, 42-57, https://doi.org/10.1016/j.rse.2014.02.015, 2014.

Pekel, J. F., Cottam, A., Gorelick, N., and Belward, A. S.: High-resolution mapping of global surface water and its long-term changes, Nature, 540, 418-422, https://doi.org/10.1038/nature20584, 2016.

Pflugmacher, D., Cohen, W. B., Kennedy, R. E., and Yang, Z.: Using Landsat-derived disturbance and recovery history and lidar to map

655 forest biomass dynamics, Remote Sensing of Environment, 151, 124-137, https://doi.org/10.1016/j.rse.2013.05.033, 2014.

Earth System
Science
Data
Open Access
Discussions

Ridd, M. K.: Exploring a V-I-S (vegetation-impervious surface-soil) model for urban ecosystem analysis through remote sensing: comparative anatomy for cities†, International Journal of Remote Sensing, 16, 2165-2185, https://doi.org/10.1080/01431169508954549, 1995.

660 Rodriguez-Galiano, V. F., Chica-Olmo, M., Abarca-Hernandez, F., Atkinson, P. M., and Jeganathan, C.: Random Forest classification of Mediterranean land cover using multi-seasonal imagery and multi-seasonal texture, Remote Sensing of Environment, 121, 93-107, https://doi.org/10.1016/j.rse.2011.12.003, 2012.

Schneider, A., Friedl, M. A., and Potere, D.: Mapping global urban areas using MODIS 500-m data: New methods and datasets based on 'urban ecoregions', Remote Sensing of Environment, 114, 1733-1746, https://doi.org/10.1016/j.rse.2010.03.003, 2010.

Schneider, A., Friedl, M. A., and Potere, D.: A new map of global urban extent from MODIS satellite data, Environmental Research Letters,
665 4, 044003, https://doi.org/10.1088/1748-9326/4/4/044003, 2009.

Schug, F., Okujeni, A., Hauer, J., Hostert, P., Nielsen, J. Ø., and van der Linden, S.: Mapping patterns of urban development in Ouagadougou, Burkina Faso, using machine learning regression modeling with bi-seasonal Landsat time series, Remote Sensing of Environment, 210, 217-228, https://doi.org/10.1016/j.rse.2018.03.022, 2018.

Shaban, M. and Dikshit, O.: Improvement of classification in urban areas by the use of textural features: the case study of Lucknow city,
670 Uttar Pradesh, International Journal of Remote Sensing, 22, 565-593, https://doi.org/10.1080/01431160050505865, 2001.

Shao, Z., Fu, H., Fu, P., and Yin, L.: Mapping Urban Impervious Surface by Fusing Optical and SAR Data at the Decision Level, Remote Sensing, 8, 945, https://doi.org/10.3390/rs8110945, 2016.

Sun, G., Kong, Y., Jia, X., Zhang, A., Rong, J., and Ma, H.: Synergistic Use of Optical and Dual-Polarized SAR Data With Multiple Kernel Learning for Urban Impervious Surface Mapping, IEEE Journal of Selected Topics in Applied Earth Observations and Remote Sensing, 12,
675 223-236, https://doi.org/10.1109/jstars.2018.2883654, 2019a.

Sun, Z., Wang, C., Guo, H., and Shang, R.: A Modified Normalized Difference Impervious Surface Index (MNDISI) for Automatic Urban Mapping from Landsat Imagery, Remote Sensing, 9, 942, https://doi.org/10.3390/rs9090942, 2017.

Sun, Z., Xu, R., Du, W., Wang, L., and Lu, D.: High-Resolution Urban Land Mapping in China from Sentinel 1A/2 Imagery Based on Google Earth Engine, Remote Sensing, 11, 752, https://doi.org/10.3390/rs11070752, 2019b.

680 Tachikawa, T., Kaku, M., Iwasaki, A., Gesch, D. B., Oimoen, M. J., Zhang, Z., Danielson, J., Krieger, T., Curtis, B., and Haase, J.: ASTER Global Digital Elevation Model Version 2 – Summary of validation results, Kim Fakultas Sastra Dan Budaya, doi: 10.1093/oxfordjournals.pubmed.a024792, 2011. https://doi.org/10.1093/oxfordjournals.pubmed.a024792, 2011.

Torres, R., Snoeij, P., Geudtner, D., Bibby, D., Davidson, M., Attema, E., Potin, P., Rommen, B., Floury, N., Brown, M., Traver, I. N., Deghaye, P., Duesmann, B., Rosich, B., Miranda, N., Bruno, C., L'Abbate, M., Croci, R., Pietropaolo, A., Huchler, M., and Rostan, F.:
685 GMES Sentinel-1 mission, Remote Sensing of Environment, 120, 9-24, https://doi.org/10.1016/j.rse.2011.05.028, 2012.

USGS: Landsat surface reflectance data, Reston, VA, Report 2015-3034, 1 pp., https://doi.org/10.3133/fs20153034, 2015.

Vermote, E., Justice, C., Claverie, M., and Franch, B.: Preliminary analysis of the performance of the Landsat 8/OLI land surface reflectance product, Remote Sensing of Environment, 185, 46-56, https://doi.org/10.1016/j.rse.2016.04.008, 2016.

Wang, Y., Liu, L., Hu, Y., Li, D., and Li, Z.: Development and validation of the Landsat-8 surface reflectance products using a MODIS-
690 based per-pixel atmospheric correction method, International Journal of Remote Sensing, 37, 1291-1314, https://doi.org/10.1080/01431161.2015.1104742, 2016.

Weng, Q.: A remote sensing-GIS evaluation of urban expansion and its impact on surface temperature in the Zhujiang Delta, China, International journal of remote sensing, 22, 1999-2014, https://doi.org/10.1080/713860788, 2001.

Weng, Q.: Remote sensing of impervious surfaces in the urban areas: Requirements, methods, and trends, Remote Sensing of Environment,
695 117, 34-49, https://doi.org/10.1016/j.rse.2011.02.030, 2012.

Wetherley, E. B., Roberts, D. A., and McFadden, J. P.: Mapping spectrally similar urban materials at sub-pixel scales, Remote Sensing of Environment, 195, 170-183, https://doi.org/10.1016/j.rse.2017.04.013, 2017.

Wu, C.: Normalized spectral mixture analysis for monitoring urban composition using ETM+ imagery, Remote Sensing of Environment, 93, 480-492, https://doi.org/10.1016/j.rse.2004.08.003, 2004.

700 Wu, C. and Murray, A. T.: Estimating impervious surface distribution by spectral mixture analysis, Remote Sensing of Environment, 84, 493-505, https://doi.org/10.1016/s0034-4257(02)00136-0, 2003.

Xie, Y. and Weng, Q.: Spatiotemporally enhancing time-series DMSP/OLS nighttime light imagery for assessing large-scale urban dynamics, ISPRS Journal of Photogrammetry and Remote Sensing, 128, 1-15, https://doi.org/10.1016/j.isprsjprs.2017.03.003, 2017.

Xu, H.: Analysis of Impervious Surface and its Impact on Urban Heat Environment using the Normalized Difference Impervious Surface
705 Index (NDISI), Photogrammetric Engineering & Remote Sensing, 76, 557-565, https://doi.org/10.14358/pers.76.5.557, 2010.

Yang, J. and He, Y.: Automated mapping of impervious surfaces in urban and suburban areas: Linear spectral unmixing of high spatial resolution imagery, International Journal of Applied Earth Observation and Geoinformation, 54, 53-64, https://doi.org/10.1016/j.jag.2016.09.006, 2017.

Yang, Y., Xiao, P., Feng, X., and Li, H.: Accuracy assessment of seven global land cover datasets over China, ISPRS Journal of
710 Photogrammetry and Remote Sensing, 125, 156-173, https://doi.org/10.1016/j.isprsjprs.2017.01.016, 2017.

Zhang, H., Lin, H., Li, Y., Zhang, Y., and Fang, C.: Mapping urban impervious surface with dual-polarimetric SAR data: An improved method, Landscape and Urban Planning, 151, 55-63, https://doi.org/10.1016/j.landurbplan.2016.03.009, 2016.

Zhang, H., Lin, H., and Wang, Y.: A new scheme for urban impervious surface classification from SAR images, ISPRS Journal of Photogrammetry and Remote Sensing, 139, 103-118, https://doi.org/10.1016/j.isprsjprs.2018.03.007, 2018a.

715 Zhang, H., Zhang, Y., and Hui, L.: Seasonal effects of impervious surface estimation in subtropical monsoon regions, International Journal of Digital Earth, 7, 746-760, https://doi.org/10.1080/17538947.2013.781241, 2014a.

Zhang, H., Zhang, Y., and Lin, H.: A comparison study of impervious surfaces estimation using optical and SAR remote sensing images, International Journal of Applied Earth Observation and Geoinformation, 18, 148-156, https://doi.org/10.1016/j.jag.2011.12.015, 2012.

Zhang, H. K. and Roy, D. P.: Using the 500 m MODIS land cover product to derive a consistent continental scale 30 m Landsat land cover
720 classification, Remote Sensing of Environment, 197, 15-34, https://doi.org/10.1016/j.rse.2017.05.024, 2017.

Zhang, L. and Weng, Q.: Annual dynamics of impervious surface in the Pearl River Delta, China, from 1988 to 2013, using time series Landsat imagery, ISPRS Journal of Photogrammetry and Remote Sensing, 113, 86-96, https://doi.org/10.1016/j.isprsjprs.2016.01.003, 2016.

Zhang, L., Zhang, M., and Yao, Y.: Mapping seasonal impervious surface dynamics in Wuhan urban agglomeration, China from 2000 to 2016, International Journal of Applied Earth Observation and Geoinformation, 70, 51-61, https://doi.org/10.1016/j.jag.2018.04.005, 2018b.

725 Zhang, X. and Liu, L.: Development of a global 30-m impervious surface map using multi-source and multi-temporal remote sensing datasets with the Google Earth Engine platform, doi: 10.5281/zenodo.3505079, 2019. https://doi.org/10.5281/zenodo.3505079, 2019.

Zhang, X., Liu, L., Chen, X., Xie, S., and Gao, Y.: Fine Land-Cover Mapping in China Using Landsat Datacube and an Operational SPECLib-Based Approach, Remote Sensing, 11, 1056, https://doi.org/10.3390/rs11091056, 2019.

Zhang, X., Liu, L., Wang, Y., Hu, Y., and Zhang, B.: A SPECLib-based operational classification approach: A preliminary test on China
730 land cover mapping at 30 m, International Journal of Applied Earth Observation and Geoinformation, 71, 83-94, https://doi.org/10.1016/j.jag.2018.05.006, 2018c.

Zhang, Y., Zhang, H., and Lin, H.: Improving the impervious surface estimation with combined use of optical and SAR remote sensing images, Remote Sensing of Environment, 141, 155-167, https://doi.org/10.1016/j.rse.2013.10.028, 2014b.

Zhou, T., Zhao, M., Sun, C., and Pan, J.: Exploring the Impact of Seasonality on Urban Land-Cover Mapping Using Multi-Season Sentinel-
735 1A and GF-1 WFV Images in a Subtropical Monsoon-Climate Region, ISPRS International Journal of Geo-Information, 7, 3, https://doi.org/10.3390/ijgi7010003, 2017.

Zhu, Z., Woodcock, C. E., Rogan, J., and Kellndorfer, J.: Assessment of spectral, polarimetric, temporal, and spatial dimensions for urban and peri-urban land cover classification using Landsat and SAR data, Remote Sensing of Environment, 117, 72-82, https://doi.org/10.1016/j.rse.2011.07.020, 2012.

740 Zhuo, L., Shi, Q., Tao, H., Zheng, J., and Li, Q.: An improved temporal mixture analysis unmixing method for estimating impervious surface area based on MODIS and DMSP-OLS data, ISPRS Journal of Photogrammetry and Remote Sensing, 142, 64-77, https://doi.org/10.1016/j.isprsjprs.2018.05.016, 2018.